Fluorescence hyperspectral imaging for live monitoring of multiple spheroids in microfluidic chips

Amélie St-Georges-Robillard,[a,b,c,d] Mathieu Masse,[a] Maxime Cahuzac,[c,d] Mathias Strupler,[a] Bishnubrata Patra,[a,c,d] Adriana Mari Orimoto,[c,d] Jennifer Kendall-Dupont,[c,d] Benjamin Péant,[c,d] Anne-Marie Mes-Masson,[c,d,e] Frédéric Leblond*[a,b,c] and Thomas Gervais*[a,b,c,d]

[a] Department of Engineering Physics, Polytechnique Montréal, C.P. 6079, Succ. Centre-ville, Montreal, Qc, H3C 3A7, Canada.
[b] Institut de génie biomédical, Polytechnique Montréal, C.P. 6079, Succ. Centre-ville, Montreal, Qc, H3C 3A7, Canada.
[c] Centre de recherche du Centre hospitalier de l'Université de Montréal, 900 St-Denis St., Montreal, Qc, H2X 0A9, Canada.
[d] Institut du cancer de Montréal, 900 St-Denis St., Montreal, Qc, H2X 0A9, Canada.
[e] Department of Medicine, Université de Montréal, 2900, boul. Edouard-Montpetit, Montreal, Qc, H3T 1J4, Canada.
* thomas.gervais@polymtl.ca, frederic.leblond@polymtl.ca.

Received: 22nd March 2018
Accepted: 27th June 2018
First published: 12th July 2018

Analyst, Volume 143, 2018, Pages 3829-3840
DOI: 10.1039/C8AN00536B
Electronic Supplementary Information (ESI) available. See DOI: 10.1039/c8an00536b

ABSTRACT

Tumor spheroids represent a realistic 3D *in vitro* cancer model because they provide a missing link between monolayer cell culture and live tissues. While microfluidic chips can easily form and assay thousands of spheroids simultaneously, few commercial instruments are available to analyze this massive amount of data. Available techniques to measure spheroid response to external stimuli, such as confocal imaging and flow cytometry, are either not appropriate for 3D cultures, or destructive. We designed a wide-field hyperspectral imaging system to analyze multiple spheroids trapped in a microfluidic chip in a single acquisition. The system and its fluorescence quantification algorithm were assessed using liquid phantoms mimicking spheroid optical properties. Spectral unmixing was tested on three overlapping spectral entities. Hyperspectral images of co-culture spheroids expressing two fluorophores were compared with confocal microscopy and spheroid growth was measured over time. The system can spectrally analyze multiple fluorescent markers simultaneously and allows multiple time-points assays, providing a fast and versatile solution for analyzing lab on a chip devices.

Introduction

Interest in multicellular tumor spheroids (MCTS, or spheroids) as a 3D *in vitro* cancer model has been steadily growing in the past decade.[1] They represent a realistic 3D cell culture model with properties that bridge the gap between monolayer cell culture and live tissues, including human biopsies, surgical specimens, or mouse xenografts.[2,3] MCTS are 3D constructs made of cells that aggregate together to form spheres of varying compactness. Contrary to monolayer (2D) cell culture, they display cell-cell and cell-matrix interactions.[2] Tumor cell lines are often able to

spontaneously form these 3D constructs when cultured in hanging droplets, low-attachment plates or passivated microfluidic chips.[4]

The microfluidics community has put considerable effort in the past ten years to develop chip-based platforms capable of forming and/or testing MCTS.[1,5–13] Some of them can be used to synthesize thousands of spheroids in one step.[14,15] Others can be used to form spheroids of different sizes utilizing a single cell suspension.[16] They can also hold (or trap) spheroids in place during medium changes or while adding/removing reagents without the risk of pipetting them out, an issue often encountered when manipulating spheroids with micropipettes in 96-well plates.[17–19]

Still, microfluidic chips are not yet fully adopted by research biologists, one of the main reasons being the complexity of use. Many microfluidic chips are designed to perform experiments efficiently but need complex pumping systems or handling.[20] Also, while microfluidic chips are able to easily produce large amounts of spheroids, very few commercial applications exist to analyze this massive amount of data. Typical techniques used by researchers consist of confocal, two-photon, and light sheet microscopy, and flow and imaging cytometry. Confocal microscopy is often used in conjunction with live/dead fluorescent markers to count the numbers of viable cells compared to dead cells in a spheroid.[10,21–23] Mohapatra *et al*. acquired spheroid fluorescence emission spectra for whole optical sections during confocal imaging.[24] While this technique offers high resolution imaging and spatial information on spheroid viability, it is limited to the first few cell layers (50-100 µm) due to limited light penetration in the 3D culture. Imaging larger fields of view also requires multiple acquisitions and image stitching.[25–27] Loss of signal-to-noise with imaging depth can prevent accurate measurement of the spheroid center response to a treatment, where necrotic, senescent, or slowly proliferating cells are present.[1]

Two-photon and light sheet microscopies circumvent this limitation by using different illumination strategies, albeit with significant drawbacks. While two-photon imaging typically uses infrared excitation to image whole spheroids, its long acquisition time for large volumes and its working distance render the technique difficult to use on multiple spheroids trapped in thick (> 5 mm) microfluidic chips.[28] Light sheet microscopy, in turn, uses structured illumination to excite a single plane in the spheroid but is not adapted to image multiple spheroids in one acquisition.[29] Other researchers have developed lens free microscopy over large fields of view, but the spectral capabilities of their systems are limited to the static (non-tunable) filters used to image fluorescent samples.[30]

Flow cytometry is also used to analyze cell populations in spheroids using fluorescent markers.[14,26] Spheroids are first digested into a single cell suspension and each cell is analyzed one at a time using fluorescence-activated cell sorting (FACS). This technique can precisely measure the proportion of cells marked by each fluorescent marker since it analyzes each cell individually. Because of the necessary spheroid digestion, FACS is a destructive analysis technique. No spatial information is obtained, contrary to confocal microscopy, and the same sample cannot be analyzed at multiple time-points. Image cytometry instruments are starting to be available for spheroid analysis,[31] but they lack the spectral resolution necessary to separate more than a few fluorophores or perform fluorescence quantification.

Wide-field fluorescence spectroscopy, seldom used in the context of 3D cell culture or microfluidics, holds several advantages that could improve spheroid analysis, namely its higher spectral resolution and its wide-field capability to image multiple samples in one acquisition. Wide-field quantitative fluorescence imaging is currently used in surgical guidance to identify

residual tumors during cancer resection.[32,33] However, since tunable filters generally have low transmission in the visible range,[34] it is a challenge to design an imaging system with a large field of view while maintaining enough sensitivity to detect the fluorescence emitted by a spheroid.

Here, we report the first use of wide-field fluorescence hyperspectral imaging to accelerate spheroid analysis while they are still trapped in a microfluidic chip. We have designed a wide-field quantitative hyperspectral imaging (HSI) system with the potential to spectrally analyze spheroids using multiple fluorescent markers in a single acquisition and in a non-destructive fashion (Fig. 1). The HSI system relies on the use of a liquid crystal tunable filter to acquire wide-field spectroscopic data of a sample with a spectral resolution of 7 nm. Because of its wide-field capability, the system can analyze multiple samples in one acquisition, enabling the study of large numbers of spheroids independently without increasing analysis time exponentially as would confocal imaging or flow cytometry. The system and its image analysis algorithm also use transmittance images of the sample to correct for its optical properties and quantify its emitted fluorescence. The proposed technique is non-destructive; samples can be analyzed at multiple time-points if the fluorescent markers used are not cytotoxic. Also, the higher spectral resolution of the HSI system enables the resolution of a larger number of fluorescent markers than a standard microscope limited by fluorescence filter cubes. Fluorophores with close emission peaks can also be resolved more easily. We also demonstrate how the HSI system can be used to analyze spheroids either made on chip (using chip B) or made using other methods (such as hanging droplets) and loaded in a microfluidic chip (chip A).

We further introduce a method to perform fluorescence quantification that is, the number of molecules of a fluorescent dye present in a spatially resolved sample. In general, that information is lost as the scattering and absorption coefficients of the sample imaged affects the fluorescence detected at the camera.[35] A custom fluorescence quantification algorithm was used to decouple the emitted fluorescence from scatterers and absorbers in the tissue using transmittance images, in order to recover the intrinsic sample fluorescence signal. Its performance is demonstrated by imaging calibrated liquid phantoms with optical properties similar to those of spheroids. Wide-field hyperspectral images of fluorescent co-culture spheroids were compared with maximum projections obtained by confocal imaging. Finally, growth curves of two cell populations forming co-culture spheroids were measured over nine days.

Overall, the HSI system is simple to use and displays superior performance when compared in terms of spectral resolution, fluorescence quantification, and analysis time with other methods and suggests that it may form the backbone of future spheroid imaging platforms.

Results

System design and characterization

The custom-built HSI system uses a tunable filter to sweep across the emission spectrum of the fluorescent sample and acquires one image per wavelength. Fig. 1A shows a concept figure where green and red fluorescent beads were placed in a single layer on a glass slide. By analyzing the emitted fluorescence intensity variations according to the measured wavelength, the beads emission spectrum can be reconstructed and the contribution of each fluorophore, unmixed.

The system is composed of two illumination paths combined towards the sample using a beamsplitter (Fig. 1B). A tungsten-halogen white light source is used to measure the transmittance

spectrum of the sample while a supercontinuum laser filtered using a laser line filter is used to excite the sample fluorescence at the chosen wavelength. An objective and relay lens form the sample's image on a highly sensitive electron-multiplying charged couple device (EMCCD) camera. A liquid crystal tunable filter sweeps across wavelengths to measure the sample transmittance and fluorescence spectra.

To measure the true emitted fluorescence intensity of a sample, precise steps are needed. Fig 2. presents an overview of the image analysis steps performed to measure and quantify the fluorescence emitted by a sample, correcting for the sample optical properties and the system response. Each step details are presented in the Experimental section.

The optical resolution and field of view of the HSI system were first characterized. A 1951 USAF resolution target was used to measure the field of view in both the x and y directions, yielding a circular field of view of 7.25 mm in diameter (see Fig 3A). This field of view is large enough to measure multiple samples in one image. The resolution target was also used to measure the resolution of the imaging system. The smallest element where a contrast difference of more than 27% between a black and a white line can be detected was observed to determine the resolution (see Fig. 3B). In both horizontal and vertical axes, the measured spatial resolution is 22.6 line pairs per millimeter.

Fluorescence quantification

The sample fluorescence was quantified with a custom algorithm according to the steps listed in Fig. 2 and using the different input data cubes described in the Experimental section. Each data cube is first normalized to the acquisition time and the gain of the camera. Fig. 3C-D shows an example of the shading correction used to correct for uneven illumination and detection responsible for a vignetting effect. The correction is shown here on the brightfield image of a single layer of fluorescent beads with diameters ranging from 300 to 355 µm. Fig. 3E-F shows the shading correction applied to the fluorescence image of the beads. While the intensity of the beads in the center of the image is clearly higher than in the periphery before the shading correction, the image after shading correction shows that the intensity is uniform. This correction allows intensity comparison of samples located in the center of the image versus the periphery as it compensates for the lower illumination/detection of peripheral samples.

A laser line tunable filter is used in the HSI system to select a specific wavelength for fluorescence excitation. This versatility comes at the cost of small out of band light contamination. An example of excitation laser bleed-through measured when a fluorescent spheroid emitting two fluorophores (enhanced Green Fluorescent Protein, eGFP, and CellTracker™ Orange, CTO) is excited at 500 nm is shown in Fig. 3G. The spheroid fluorescence intensity (peaks at 515 and 575 nm) is similar to the bleed-through intensity (three peaks around 625 nm). Spectral unmixing is used to remove this bleed-through and to separate the contribution of each fluorophore to the spheroid fluorescence. Because of the varying thickness of the PDMS between samples, the intensity of the excitation laser bleed-through varies and cannot be simply subtracted. Here, the spectral unmixing algorithm considers the spectral shape of the bleed-through to be removed (see Fig. 3G). Hyperspectral images in Fig. 3H illustrate the removal of the bleed-through from a region of interest containing an eGFP-expressing and CTO-stained spheroid loaded into a well of microfluidic chip A (see Experimental section for the details on the two microfluidic chips used throughout this work). Because of the low intensity of CTO fluorescence compared to eGFP, it would be impossible to detect CTO with a conventional fluorescence microscope. Fig. 3G-H

shows how it was possible to use the HSI system and spectral unmixing to separate the CTO contribution from the eGFP fluorescence and illustrates the potential of hyperspectral imaging in spheroid-based research.

The fluorescence quantification performance of this imaging system was verified using liquid optical phantoms mimicking the optical properties of tumor spheroids. Here, since spheroids do not contain strong absorbers, such as hemoglobin, their absorbance is found to be negligible compared to their scattering coefficient.[36,37] The fluorophore of interest expressed by the eGFP modified cells used to make spheroids was simulated using fluorescein diluted in a 0.1 M TRIS-HCl (Tris(hydroxymethyl)aminomethane hydrochloride) buffer at pH 8. This buffer and pH was selected to position fluorescein's maximum emission peak at 514 nm when dissolved. Lipid emulsion Intralipid® 20% was used to simulate the scattering properties of spheroids.[38] Thirty phantoms were fabricated, introduced in a 1 mm-pathlength optical glass cuvette and their fluorescence was measured using the HSI system. The fluorescence images of each phantom were then analyzed to find the best α (see equation 1) to quantify the fluorescence, similar to what Valdés *et al.* presented in their work.[39] Fig. 4A shows the corrected fluorescence intensity at 515 nm of optical phantoms with varying fluorophore concentrations, [F], and reduced scattering coefficients, μ_s'. The images shown are those obtained after performing all image analysis steps using $\alpha = 0$ to measure the corrected fluorescence of the phantom without any quantification. As the fluorophore concentration increases, the detected fluorescence intensity increases linearly, as expected. Similarly, as the reduced scattering coefficient increases, the detected fluorescence intensity also increases, while the transmittance of the phantom decreases (Fig. 4B). Fig. 4C shows the quantified fluorescence images of each fluorophore where, for a specific fluorescein concentration, the quantified fluorescence is the same.

The phantom or imaged sample geometry will affect the fluorescence intensity measured at the camera by an imaging system in transmission mode. Here, as the scattering coefficient of the phantoms is increased, their transmittance also decreases. Meanwhile, the measured fluorescence increases. This seems counter-intuitive, as one could think the more scattering the sample is, the more light will be scattered away from the camera. Our results can be explained by a greater number of photons trapped inside the sample at higher concentrations of scatterers, yielding a higher amount of excited fluorophore molecules and a higher detected fluorescence intensity at the camera. This observation highlights why the geometry of the optical phantom used to mimic the biological specimen is important.

Fig. 4D shows the fluorescence intensity summed from 500 to 720 nm of a square region of interest of 6 by 6 pixels selected in the middle of the images. Corrected fluorescence ($\alpha = 0$) and quantified fluorescence ($\alpha = -0.34$) are presented. The insert in Fig. 4D shows the optimization of the geometric quantification factor α. The large dispersion of corrected fluorescence intensity values prevents accurate fluorescence quantification ($R^2 = 0.67$ for a linear fit) while quantified fluorescence yields a linear fit where $R^2 = 0.97$.

For phantoms where $\mu_s' = 7.5$ cm^{-1}, noise is introduced into the quantified fluorescence images because of the low transmittance of the sample, illustrating the limit of this method for fluorescence quantification at very low transmittances. This phantom experiment also shows how transmittance of finite phantoms can also be used to quantify fluorescence, similarly to how reflectance is used in the case of semi-infinite phantoms or tissues.[40]

Imaging co-culture spheroids

The system's performance in fluorescence imaging of 3D biological samples was first tested by comparing hyperspectral and confocal images of the same spheroids. Spheroids were made using the hanging droplet method[41] and different ratios of eGFP-OV1946 cells and mCardinal-OV90 cells and then loaded in chip A (Fig. 5A). Spheroids were first imaged using confocal microscopy followed by hyperspectral imaging and regions of interest are presented in Fig. 5B. Visual comparison shows that, while the spatial resolution of the hyperspectral system is lower, the same features can be observed in the spheroids. Even if HSI images have a lower resolution than confocal imaging, we can still observe that the fluorescent cells originating from two different cell lines do not mix homogeneously while forming the spheroid. Instead, they tend to aggregate in separate volumes.

In a second experiment, we used fluorescent clones produced from the same cell line to form homogeneously mixed co-culture spheroids. Since the cell line OV1946 is known for its genetic instability,[42] the stable clone selection process done after transfection with fluorescent proteins should produce subclones of varying growth behaviors. To assess if hyperspectral imaging could measure these even in co-culture spheroids where the cells are mixed homogeneously, spheroids were made in chip B using mCherry- and eGFP-expressing OV1946 cells at the following initial ratios: 100:0, 75:25, 25:75, and 0:100. 24 spheroids were imaged in a single acquisition and their subpopulations' fluorescence was measured every day for 9 days. The experiment was repeated 3 times. Fig. 6A shows the microfluidic chip used in this experiment. The bottom row images in Fig. 6A show that, contrary to spheroids shown in Fig. 5B, cells in co-culture spheroids formed using fluorescent subclones of the same cell line are homogeneously mixed. Fig. 6B shows the brightfield image of 24 spheroids made in chip B using the initial ratio 25:75 (eGFP:mCherry). Blue squares are added to represent the maximum number of spheroids that it would be possible to image in a single acquisition using the hyperspectral system. For this particular well size, 60 spheroids could be imaged in the 7.25 mm-diameter field of view. Fig 6C shows the corrected fluorescence at 515 nm (eGFP's emission peak) and 610 nm (mCherry's emission peak) while Fig. 6D shows the transmittance image at 515 nm of the same 24 spheroids. The spheroids' transmittance varies between 20% and 30%, depending on their size. Here, α was fixed at 0 during the image analysis steps to show the spheroid corrected fluorescence. Acquisition times for confocal and hyperspectral imaging are similar ($\approx$ 5 minutes per acquisition). But since the wide-field capabilities of the HSI system allows up to 60 spheroids in the same field of view, acquisition times are up to 60 times faster using our system.

Fig. 6E shows the percentage of mCherry-OV1946 cells over time for each initial ratio. Fig. 6F shows the same curves normalized to day 1, since spheroids are formed in 24 h. This figure clearly shows that, from day 1 to 9, their growth rate is linear and nearly identical for each initial ratio. Contrary to mCherry-OV1946 cells, eGFP-OV1946 cells presented a different growth behavior (Fig. 6G). While each experiment repetition yielded very similar growth curves for mCherry cells, as highlighted by the small error bars, eGFP cells proliferated more erratically in each repetition. Their growth also reached a plateau around day 4, contrary to mCherry cells. Fig. 6H shows that eGFP cells that formed initially 25% of a spheroid grew more than eGFP cells that formed 100%, even if the total amount of cells in the spheroids was the same. In 200 to 300-µm spheroids, eGFP cell growth is reduced in the presence of other eGFP cells.

By showing how cell subpopulations behave differently in co-culture spheroids, Fig. 6E-H illustrates how quantifying co-culture spheroid fluorescence using HSI is an ideal method to

measure cell populations independently and non-destructively while the spheroids are still trapped in a microfluidic chip. Also, the hyperspectral system was found to be more versatile in terms of choosing which and how many fluorophores to image since the shape of the whole fluorescence spectrum is known for each pixel of the image, while confocal imaging is limited to the filter cubes or spectral capability of the confocal microscope.

Since the samples are transilluminated, a larger volume of the spheroids can be analyzed, providing an advantage over confocal microscopy (usually used in epi-illumination). In confocal microscopy, the pinholes used to create the optical sectioning limit the detected intensity and light penetration in 3D cultures.[25–27] Also, the volume sampled in a 3D specimen by an imaging system depends on the illumination and detection configuration. Epi-illumination imaging systems mostly sample one side of the spheroids, since illumination and detection are performed on the same side. This technique will be more sensitive to the effect of a drug on the outer layer of a spheroid. Transillumination, on the other hand, will sample more of the spheroid volume since illumination is on the other side of the sample compared to detection.

Experimental

Hyperspectral imaging system

The custom-built spectroscopic imaging system presented here is detailed in Fig. 1B. It uses a white light lamp for transmittance measurements and a filtered supercontinuum laser that allows the user to vary the fluorescence excitation wavelength between 400 nm and 720 nm. A liquid crystal tunable filter is used to perform a wavelength-sweep and acquire spectroscopic data. More precisely, a tungsten-halogen white light source (HL-2000, Ocean Optics, USA) is used to illuminate the sample from below, using a Köhler illumination setup, where two irises independently control the area illuminated and the illumination irradiance. In a second illumination branch, a supercontinuum laser (Fianium, NKT Photonics, Denmark) coupled to a laser line tunable filter (LLTF, Photon etc, Canada) and a mode scrambler is used to excite the fluorescence of the sample. The two illumination branches are combined using a 50:50 cube beamsplitter (BS013, Thorlabs, USA). A fixed focal length objective (59-871, Edmund Optics, USA) and a Steinheil triplet lens (67-422, Edmund Optics) acting as a relay lens are used to image the sample on an electron-multiplying charged coupled device (EMCCD) camera (HNü 512, Nüvü Caméras, Canada) thermoelectrically cooled to -85°C. A liquid crystal tunable filter (LCTF) with a bandwidth of 7 nm (VariSpec VIS, Perkin-Elmer, USA) is placed between the relay lens and the EMCCD to acquire spectroscopic data at each pixel of the image. A 500 nm (or 550 nm) shortpass filter (FESH0500 or FESH0550, Thorlabs) filters out the excitation laser light to remove any unwanted harmonics due to the LLTF. A 500 nm (or 550 nm) longpass filter (FELH0500 or FELH0550, Thorlabs) is placed after the objective to remove the excitation laser from the acquired images.

Data acquisition

Two excitation wavelengths are used in this work: 480 nm and 530 nm. To acquire a spectroscopic image of the microfluidic chip placed in the sample plane, the LLTF is set to 480 nm (or 530 nm) and a custom LabVIEW 2014 (National Instruments, USA) software[33] is used to sweep the LCTF from 500 to 720 nm (or 560 to 720 nm) and acquire an image every 5 nm. The resulting image cube is a 3D matrix of 512 by 512 pixels by 45 (or 33) wavelengths.

To apply the image analysis steps, the acquisition of several data cubes is required for each sample. First, three acquisitions are made using the imaging system in fluorescence mode, all at the same acquisition time and gain: 1) a fluorescence image (while the sample is present in the sample plane); 2) a dark noise image (camera shutter closed); 3) a bleed-through image of the laser (no sample present). A similar set of data cubes is acquired using the white light source to measure the transmittance of the sample. A typical acquisition of brightfield and fluorescence (480 nm excitation) data cubes takes 149.85 s (2.5 min). Table 1 summarizes the different data cubes needed for the subsequent image analysis and shows the typical acquisition parameters used to measure the fluorescence of spheroids trapped in a microfluidic chip.

After any changes to the imaging system (such as optical alignment or optical parts for example), a series of calibration steps are performed to characterize the imaging system. First, the transmittance of a USAF 1951 resolution target (R3L3S1N, Thorlabs) is measured between 500 and 720 nm using the white light source. This acquisition is used to measure the field of view and the spatial resolution of the system. A set of uniformly fluorescent Chroma slides (92001, Chroma, USA) is then measured in fluorescence and brightfield modes to characterize the spatial intensity variations due to the imaging system's optical design. A shading correction is applied for each sample and its performance is assessed using uniformly fluorescent beads (UVPMS-BR-1.090 300-355um, Cospheric LLC, USA). Finally, the excitation laser power density for both excitation wavelengths is measured at the sample plane using a power meter (S121C, Thorlabs).

Image analysis

To analyze hyperspectral images and quantify a sample's fluorescence, a custom algorithm was developed. Fluorescence spectra acquired for each sample are processed in MATLAB R2015a (The MathWorks, Inc., USA) to extract quantified data according to the steps listed in Fig. 2. Each data cube is first normalized to the acquisition time and the gain of the EMCCD camera, as those parameters are calibrated linearly by the camera's manufacturer. Dark noise, measured for each acquisition time and gain parameter set (see Table 1), is then subtracted from the fluorescence and brightfield images of the studied sample.

A shading correction is applied to the sample images to correct for uneven illumination and detection due to the system's optical design. Using fluorescence and brightfield images of the uniformly fluorescent orange Chroma slide acquired during the calibration steps, a compensation matrix is calculated by first smoothing the images and then normalizing them to their maximal values. For fluorescence measurements, a single fluorescence compensation matrix is calculated using the image at the emission peak maximum (555 nm), while a brightfield compensation matrix is calculated at each wavelength of the brightfield measurements. The shading correction is applied to the fluorescent images by dividing the images at each wavelength by the fluorescence compensation matrix and to the brightfield images by dividing the images at each wavelength by their corresponding brightfield compensation matrix.

The transmittance of the sample is then calculated by dividing its brightfield data cube by the brightfield images acquired while no sample is present ("System transmission" data cube from Table 1). The region of interest (ROI) to further study the fluorescence of the sample is then defined.

If precise fluorescence quantification is needed, a quantification step can be performed to correct for the optical properties of the sample that are impacting the fluorescence measured by

the camera. To do so, the fluorescence data cube is divided by the transmittance image according to a modified normalization quantification algorithm based on:[39]

$$\boldsymbol{\Phi}^{\boldsymbol{Ratio}}(\boldsymbol{\lambda}) = \frac{\boldsymbol{\Phi}^{\boldsymbol{Fluo}}(\boldsymbol{\lambda})}{(\boldsymbol{\Phi}_{\boldsymbol{m}}^{\boldsymbol{Trans}})^{\boldsymbol{\alpha}}} \qquad (1)$$

where $\boldsymbol{\Phi}^{\boldsymbol{Ratio}}(\boldsymbol{\lambda})$ is the quantified fluorescence spectrum, $\boldsymbol{\Phi}^{\boldsymbol{Fluo}}(\boldsymbol{\lambda})$ is the fluorescence spectrum after shading correction, $\boldsymbol{\Phi}_{\boldsymbol{m}}^{\boldsymbol{Trans}}$ is the transmittance intensity at the fluorophore emission peak, and α is empirically determined using liquid optical phantoms of known optical properties.

In each ROI, a spectral unmixing is performed to 1) remove the excitation laser bleed-through and 2) extract the contribution of each fluorophore present in the sample. The spectral unmixing is done by solving a nonnegative linear least-square problem. The basis spectra are previously acquired experimental fluorescence spectra of each fluorophore, and an average spectrum extracted from the same region of interest but using the bleed-through data cube ("laser bleed-through" from Table 1). Since the intensity of the bleed-through is acquired while no sample is present and the PDMS affects the intensity of the bleed-through contamination when the fluorescence of the sample is acquired, the bleed-through is removed through spectral unmixing instead of simply subtracted from the fluorescence data cube.

Optical phantoms

Optical phantoms mimicking spheroid optical properties were made of fluorescein (M422-05, Avantor, USA) to simulate eGFP and Intralipid® 20% (2B6023, Baxter, Canada) as a light scatterer. Fluorescein was solubilized in a 0.1 M TRIS-HCl (Tris(hydroxymethyl)aminomethane hydrochloride) buffer (TRIS base: 600-125-IK, Wisent Inc., Canada, and HCl: 3750.1-32, Ricca Chemical Company, USA) made at pH 8. Fluorescein concentrations of 0.625, 1.25, 2.5, 5, and 10 µg/ml and reduced scattering coefficients at 515 nm of 0.5, 1, 1.5, 3, 5, and 7.5 cm^{-1} were combined to make 30 different phantoms. These liquid phantoms were introduced in a 1 mm-pathlength cuvette made of optical glass (G101, Azzota, USA).

Microfluidic chips

Two microfluidic chips were used to form spheroids on chip and/or hold them in place to image them. Chip A, shown in Fig. 5A, is based on Astolfi *et al.*[26] and is composed of a main channel and five wells. A maximum of five spheroids previously made using other techniques can be loaded in the chip and trapped in the wells. The second microfluidic chip used, Chip B, shown in Fig. 6D, is based on a design by Patra *et al.*[14] and is used to form 120 spheroids directly on chip using a cell suspension. Spheroids made using this microfluidic chip can then be easily exposed to drugs without accidentally releasing them from the wells. The microfluidics chips used in each experiment were chosen according to how the spheroids were formed, whether on chip or using the hanging droplet method[41].

Chip A consists of 5 wells placed under a main channel. Each well is 600 x 600 μm^2 and 500 µm in height. The top channel is 600 µm wide by 600 µm in height. Poly(methyl methacrylate) (PMMA) molds were micromachined by a computerized numerical control (CNC) machine (EMCO PC Mill 55, EMCO GmbH, Austria); one for the main channel and the wells and the other for the layer containing the inlets and outlets. Degassed liquid PDMS (Sylgard® 184 silicone elastomer kit, Dow Corning, USA) mixed at 10:1 ratio was then poured into the two molds and cured in an oven at 80 °C for 1 h. The two layers were then exposed to an atmospheric plasma for

30 s and then bonded together. Hollow nylon cylinders (91145A138, McMaster-Carr, USA) were then inserted in the main channel inlets. In this design, spheroids made using the hanging droplet method were introduced in the chip inlet. Careful aspiration of the fluid at the outlet was then used to position the spheroids over the wells and let them sediment.

Chip B was also made using CNC micromachined molds and PDMS. It consists of a main channel containing 5 series of 24 wells. Each well is 500 x 500 μm^2 and 500 µm in height. The top channel is 2 mm wide and 500 µm in height. The circular inset of Fig. 1B shows a brightfield image of a section of the chip where 24 wells contain spheroids formed on chip.

Both microfluidic chip designs were prepared for cell culture by first introducing 100% ethanol to remove any bubbles in the chips. 70% ethanol was then introduced for 10 minutes to sterilize the chips. A solution of sterilized triblock copolymer (10 mg/mL, Pluronic® F-108, 542342, Sigma-Aldrich, USA) was then incubated in the chip at 37 °C for at least 1 h or overnight to prevent cell adhesion on the channel walls and inside the wells. Chips were then re-sterilized using 70% ethanol for 10 minutes and chips were finally completely rinsed and filled with sterile Hank's Balanced Salt Solution (HBSS, 311-516-CL, Wisent Inc.) supplemented with 600 µg/L amphotericin B (450-105-QL, Wisent Inc.) and 55 mg/L gentamicin (450-135-XL, Wisent Inc.) and then stored for future use at room temperature in a sterile humidity chamber (plastic box containing a tissue moistened with sterile water) to prevent HBSS evaporation.

Spheroid culture

Two high grade serous epithelial ovarian cancer cell lines, OV1946[42] and OV90,[43] were previously established from patient ascites in our laboratory at the Centre de recherche du CHUM. The two cell lines were transiently transfected with either an eGFP plasmid (pEGFP-N1, 6085-1, Clontech Laboratories Inc., USA), a mCardinal plasmid[44] (mCardinal-N1, #54590, Addgene, USA), or a mCherry plasmid (mCherry2-N1, #54517, Addgene). Plasmids mCardinal-N1 and mCherry2-N1 were gifts from Michael Davidson. To generate stable clones, successfully transfected cells were selected with 500 µg/ml G418 (Geneticin®, 10131-035, Thermo Fisher Scientific, USA) and single clones were selected by limiting dilution. Available stable clones were eGFP-expressing and mCherry-expressing OV1946 cells, and mCardinal-expressing OV90 cells.

In a first experiment, co-culture spheroids were formed using the hanging droplet method described previously.[41] Briefly, cell suspensions of eGFP-OV1946 (passage 8) and mCardinal-OV90 (passage 8) in complete OSE medium [OSE medium (316-030-CL, Wisent Inc.) supplemented with 10% FBS (080-150, Wisent Inc.), 55 mg/L gentamicin (450-135-XL, Wisent Inc.), and 600 µg/L amphotericin B] with 500 µg/mL G418 were used to obtain a total of 2.5 x 10^5 cells/ml at different ratios: 100:0, 90:10, 75:25, 50:50, 25:75, 10:90, and 0:100. Then, 16 µL of the different cell suspensions were carefully pipetted onto the inner side of the cover of a 150 mm petri dish (CA25383-103, VWR, Canada) to form droplets. The cover was gently placed on the dish containing 15 ml of phosphate buffered saline (PBS, 311-012-LL, Wisent Inc.) to prevent dehydration of the droplets. Petris were placed in an incubator at 37 °C and 5% CO_2. The spheroids were harvested at day 7 and carefully loaded into the wells of chip A for hyperspectral and confocal imaging.

Co-culture spheroids made from different ratios of two fluorescent cell lines were formed directly inside chip B. Cell suspensions of 9 x 10^5 cells/mL containing various ratios of eGFP-OV1946 cells (passage 90) and mCherry-OV1946 cells (passage 34) were prepared in complete OSE medium with G418 (500 µg/mL). Studied ratios of eGFP- versus mCherry-expressing cells

were 100:0, 75:25, 25:75, and 0:100. About 600 µL of cell suspension were introduced in the main channel of each microfluidic chip to form spheroids in 24 h. The culture medium, complete OSE medium without phenol [using OSE medium without phenol (316-031-CL, Wisent Inc.)] supplemented with 500 µg/mL G418, was replaced every 24 h by introducing 70 µL of new medium at the inlet and removing 3 x 20 µL of medium at the outlet, three times. Medium without phenol was used to avoid autofluorescence due to the phenol. Between medium changes, the microfluidic chips were kept in a sterile humidity chamber in an incubator at 37 °C and 5% CO_2. 24 h after cell seeding, the cells aggregated and formed one spheroid per well without adhering to the PDMS surface. When necessary, spheroids trapped in the microfluidic chip were stained with fluorescent markers. A 5 µM solution of CellTracker™ Orange CMTMR (C2927, Thermo Fisher Scientific) in HBSS was added to the chip and placed in an incubator at 37 °C and 5% CO_2 for 1 hour. The staining solution was then rinsed with fresh medium.

Confocal imaging

Confocal imaging was performed on co-culture spheroids trapped in Chip A. Images were acquired on a Leica TCS-SP5 inverted microscope (Leica Microsystems, Germany) using a HC PL FLUOTAR 20x/0.50 dry objective. Excitation system was performed using the 488 nm line of an argon laser for eGFP, and the 561 nm diode-pumped solid state (DPSS) laser for mCardinal using a sequential acquisition at a scan speed of 400 Hz. Spectral detector mirrors were set for each fluorophore to avoid excitation and emission crosstalk: 500 nm-550 nm for eGFP; 598 nm-700 nm for mCardinal. Z-stack images were acquired with an 8 µm step size and maximum projections were performed using the Las-AF software. Final images are 8 bits and 512 x 512 pixels with a zoom factor of 1.5.

Conclusion

We presented a custom designed wide-field HSI system based on a liquid crystal tunable filter to image tumor spheroids while they are trapped in a microfluidic chip. It circumvents the typical limitations of confocal microscopy: acquisition time and light penetration depth. Its wide-field capability allows the simultaneous measurement of up to 60 spheroids in a single acquisition. Furthermore, the spectral resolution of the HSI system enables a wide choice of fluorophores to image. The acquisition of the whole fluorescence spectrum for every pixel of the image increases the discriminating power for spectral unmixing and allows the study of fluorophores with more similar spectra than conventional filter-based methods. Also, because of the supercontinuum laser and its laser line filter, the excitation wavelength can be adjusted for photoactivable fluorophores.[45] The HSI system permits non-destructive measurements of 3D cell cultures, unlike flow cytometry. This becomes an important advantage when studying the evolution of a spheroid response to a molecular agent at multiple time-points. Although the spheroid work presented here relates to ovarian cancer, any cancer whose cells spontaneously form spheroids in low attachment environment can be studied as well as small tissues such as organoids[46], embryos[47], and microdissected tissues[26].

Conflicts of interest

There are no conflicts of interest to declare.

Acknowledgements

The authors acknowledge Michael Jermyn and Lucas Aubé for Matlab functions, and Yoann Gosselin, Karl St-Arnaud, and Leticia M. Angulo-Rodríguez for Labview programs. We are grateful to Benoît Bourassa-Moreau for fruitful discussions on light propagation, and to Aurélie Cleret-Buhot from the Cell Imaging Facility at the Centre de recherche du Centre hospitalier de l'Université de Montréal for help with confocal imaging. This work was supported by the National Sciences and Engineering Research Council of Canada (NSERC), by the Canada Foundation for Innovation, and by a partnered Cancer Research Society and Ovarian Cancer Canada (#20103) grant. Authors acknowledge CMC Microsystems. A.S.R. acknowledges scholarships from NSERC, and the Fonds de recherche du Québec - Nature et technologies.

References

1 F. Hirschhaeuser, H. Menne, C. Dittfeld, J. West, W. Mueller-Klieser and L. A. Kunz-Schughart, *J. Biotechnol.*, 2010, **148**, 3–15.

2 F. Pampaloni, E. G. Reynaud and E. H. K. Stelzer, *Nat. Rev. Mol. Cell Biol.*, 2007, **8**, 839–45.

3 S. Jeong, J. Lee, Y. Shin, S. Chung and H. Kuh, *PLoS One*, 2016, **11**, e0159013.

4 R.-Z. Lin and H.-Y. Chang, *Biotechnol. J.*, 2008, **3**, 1172–84.

5 V. van Duinen, S. J. Trietsch, J. Joore, P. Vulto and T. Hankemeier, *Curr. Opin. Biotechnol.*, 2015, **35**, 118–126.

6 N. Kashaninejad, M. Nikmaneshi, H. Moghadas, A. Kiyoumarsi Oskouei, M. Rismanian, M. Barisam, M. Saidi and B. Firoozabadi, *Micromachines*, 2016, **7**, 130.

7 N. Rousset, F. Monet and T. Gervais, *Sci. Rep.*, 2017, **7**, 245.

8 R. Vadivelu, H. Kamble, M. Shiddiky and N.-T. Nguyen, *Micromachines*, 2017, **8**, 23.

9 J. Ruppen, F. D. Wildhaber, C. Strub, S. Hall, T. Geiser, R. A. Schmid and O. T. Guenat, *Lab Chip*, 2015, **15**, 3076–3085.

10 S.-B. Huang, S.-S. Wang, C.-H. Hsieh, Y. C. Lin, C.-S. Lai and M.-H. Wu, *Lab Chip*, 2013, **13**, 1133–43.

11 S. Agastin, U.-B. T. Giang, Y. Geng, L. A. Delouise and M. R. King, *Biomicrofluidics*, 2011, **5**, 24110.

12 L. Yu, C. Ni, S. M. Grist, C. Bayly and K. C. Cheung, *Biomed. Microdevices*, 2015, **17**, 33.

13 C. Y. Chan, P.-H. Huang, F. Guo, X. Ding, V. Kapur, J. D. Mai, P. K. Yuen and T. J. Huang, *Lab Chip*, 2013, **13**, 4697.

14 B. Patra, C.-C. Peng, W.-H. Liao, C.-H. Lee and Y.-C. Tung, *Sci. Rep.*, 2016, **6**, 21061.

15 H. Hardelauf, J.-P. Frimat, J. D. Stewart, W. Schormann, Y.-Y. Chiang, P. Lampen, J. Franzke, J. G. Hengstler, C. Cadenas, L. A. Kunz-Schughart and J. West, *Lab Chip*, 2011, **11**, 419–28.

16 M. Marimuthu, N. Rousset, A. St-Georges-Robillard, M. A. Lateef, M. Ferland, A.-M. Mes-Masson and T. Gervais, *Lab Chip*, 2018, **18**, 304–314.

17 O. Frey, P. M. Misun, D. A. Fluri, J. G. Hengstler and A. Hierlemann, *Nat. Commun.*, 2014, **5**, 4250.

18 K. Kwapiszewska, A. Michalczuk, M. Rybka, R. Kwapiszewski and Z. Brzózka, *Lab Chip*, 2014, **14**, 2096–104.

19 A. R. Brunet, F. Labelle, P. Wong and T. Gervais, *Sensors*, 2017, **17**, 2271.

20 A. Junaid, A. Mashaghi, T. Hankemeier and P. Vulto, *Curr. Opin. Biomed. Eng.*, 2017, **1**, 15–22.

21 I. Ahonen, M. Åkerfelt, M. Toriseva, E. Oswald, J. Schüler and M. Nees, *Sci. Rep.*, 2017, **7**, 6600.

22 L. E. Smith, R. O. D. Smallwood and S. Macneil, *Microsc. Reasearch Tech.*, 2010, **73**, 1123–1133.

23 N. J. Martinez, S. A. Titus, A. K. Wagner and A. Simeonov, *Expert Opin. Drug Discov.*, 2015, **0441**, 1–15.

24 S. Mohapatra, S. Nandi, R. Chowdhury, G. Das, S. Ghosh and K. Bhattacharyya, *Phys. Chem. Chem. Phys.*, 2016, **18**, 18381–18390.

25 T. Das, L. Meunier, L. Barbe, D. Provencher, O. T. Guenat, T. Gervais and A.-M. M. Mes-Masson, *Biomicrofluidics*, 2013, **7**, 011805-1-011805-15.

26 M. Astolfi, B. Péant, M. A. Lateef, N. Rousset, J. Kendall-Dupont, E. Carmona, F. Monet, F. Saad, D. Provencher, A.-M. Mes-Masson and T. Gervais, *Lab Chip*, 2016, **16**, 312–325.

27 J. Kang, D. W. Lee, H. J. Hwang, S.-E. Yeon, M.-Y. Lee and H.-J. Kuh, *Lab Chip*, 2016, **16**, 2265–2276.

28 M. Makale, M. McElroy, P. O'Brien, R. M. Hoffman, S. Guo, M. Bouvet, L. Barnes, E. Ingulli and D. Cheresh, *J. Biomed. Opt.*, 2009, **14**, 024032.

29 B. Patra, Y.-S. Peng, C.-C. Peng, W.-H. Liao, Y.-A. Chen, K.-H. Lin, Y.-C. Tung and C.-H. Lee, *Biomicrofluidics*, 2014, **8**, 052109.

30 A. Ozcan and E. McLeod, *Annu. Rev. Biomed. Eng.*, 2016, **18**, 77–102.

31 S. Kessel, S. Cribbes, O. Déry, D. Kuksin, E. Sincoff, J. Qiu and L. L.-Y. Chan, *SLAS Technol. Transl. Life Sci. Innov.*, 2016, **22**, 454–465.

32 J. P. Angelo, M. van de Giessen and S. Gioux, *Biomed. Opt. Express*, 2017, **8**, 5113–5126.

33 M. Jermyn, Y. Gosselin, P. A. Valdes, M. Sibai, K. Kolste, J. Mercier, L. Angulo, D. W. Roberts, K. D. Paulsen, K. Petrecca, O. Daigle, B. C. Wilson and F. Leblond, *Biomed. Opt. Express*, 2015, **6**, 5063.

34 J. M. Lerner, N. Gat and E. Wachman, in *Current protocols in cytometry, Unit 12.20*, 2010.

35 R. B. Saager, D. J. Cuccia, S. Saggese, K. M. Kelly and A. J. Durkin, *J. Biomed. Opt.*, 2011, **16**, 126013.

36 V. P. Wallace, A. K. Dunn, M. L. Coleno and B. J. Tromberg, in *Methods in Cellular Imaging*, ed. A. Periasamy, Springer, New York, USA, 2001, pp. 180–199.

37 P. Hargrave, P. W. Nicholson, D. T. Delpy and M. Firbank, *Phys. Med. Biol.*, 1996, **41**, 1067–72.

38 S. T. Flock, S. L. Jacques, B. C. Wilson, W. M. Star and M. J. van Gemert, *Lasers Surg. Med.*, 1992, **12**, 510–9.

39 P. A. Valdés, F. Leblond, A. Kim, B. C. Wilson, K. D. Paulsen and D. W. Roberts, *Opt. Lett.*, 2012, **37**, 1817–9.

40 R. S. Bradley and M. S. Thorniley, *J. R. Soc. Interface*, 2006, **3**, 1–13.

41 M. Zietarska, C. M. Maugard, A. Filali-Mouhim, M. Alam-Fahmy, P. N. Tonin, D. M. Provencher and A.-M. Mes-Masson, *Mol. Carcinog.*, 2007, **46**, 872–885.

42 V. Ouellet, M. Zietarska, L. Portelance, J. Lafontaine, J. Madore, M.-L. Puiffe, S. L. Arcand, Z. Shen, J. Hébert, P. N. Tonin, D. M. Provencher and A.-M. Mes-Masson, *BMC Cancer*, 2008, **8**, 152.

43 D. M. Provencher, H. Lounis, L. Champoux, M. Tétrault, E. N. Manderson, J. C. Wang, P. Eydoux, R. Savoie, P. N. Tonin and A.-M. Mes-Masson, *Vitr. Cell. Dev. Biol. - Anim.*, 2000, **3**, 357–361.

44 J. Chu, R. D. Haynes, S. Y. Corbel, P. Li, E. González-González, J. S. Burg, N. J. Ataie, A. J. Lam, P. J. Cranfill, M. A. Baird, M. W. Davidson, H. L. Ng, K. C. Garcia, C. H. Contag, K. Shen, H. M. Blau and M. Z. Lin, *Nat. Methods*, 2014, **11**, 572–578.

45 F. V. Subach, G. H. Patterson, S. Manley, J. M. Gillette, J. Lippincott-Schwartz and V. V. Verkhusha, *Nat. Methods*, 2009, **6**, 153–159.

46 A. Fatehullah, S. H. Tan and N. Barker, *Nat. Cell Biol.*, 2016, **18**, 246–254.

47 K. Chung, Y. Kim, J. S. Kanodia, E. Gong, S. Y. Shvartsman and H. Lu, *Nat. Methods*, 2011, 8, 171–6.

Figures

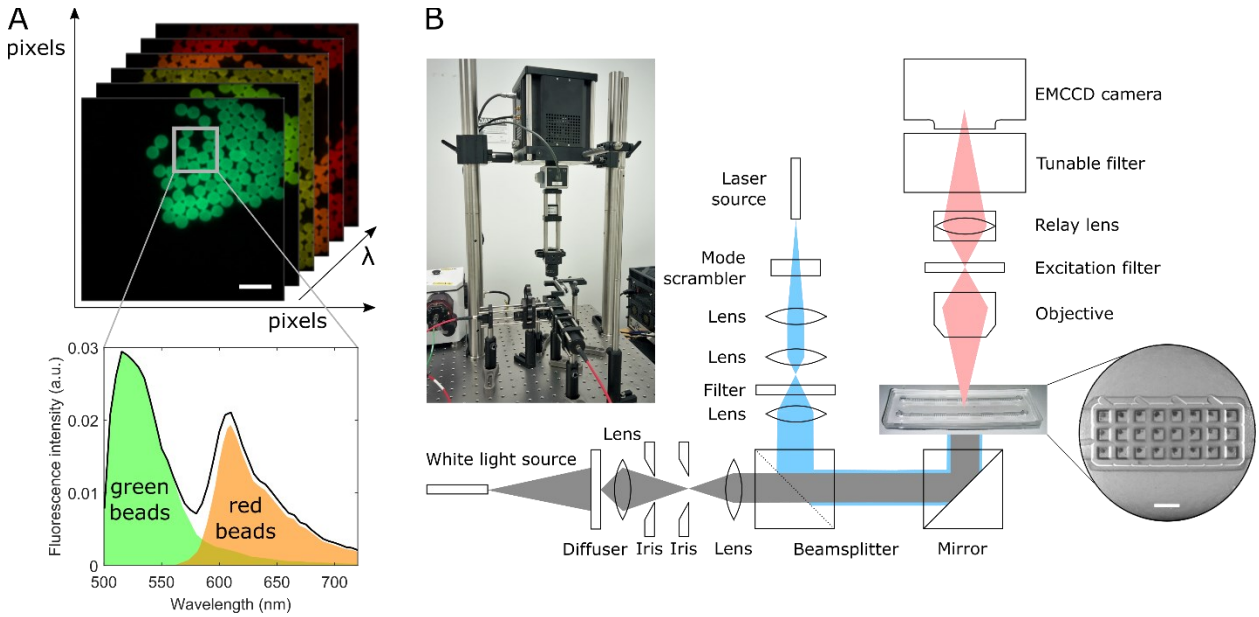

Figure 1. Hyperspectral imaging. (A) Concept figure of hyperspectral imaging of a single layer of green and red fluorescent beads and the average spectrum from the pixels inside the gray rectangle. Unit a.u. is for arbitrary units. Scale bar = 1 mm. (B) Hyperspectral imaging system diagram. Circular inset shows microfluidic chip B containing 24 wells where spheroids were formed and trapped. Scale bars = 1 mm. Photograph shows the imaging system.

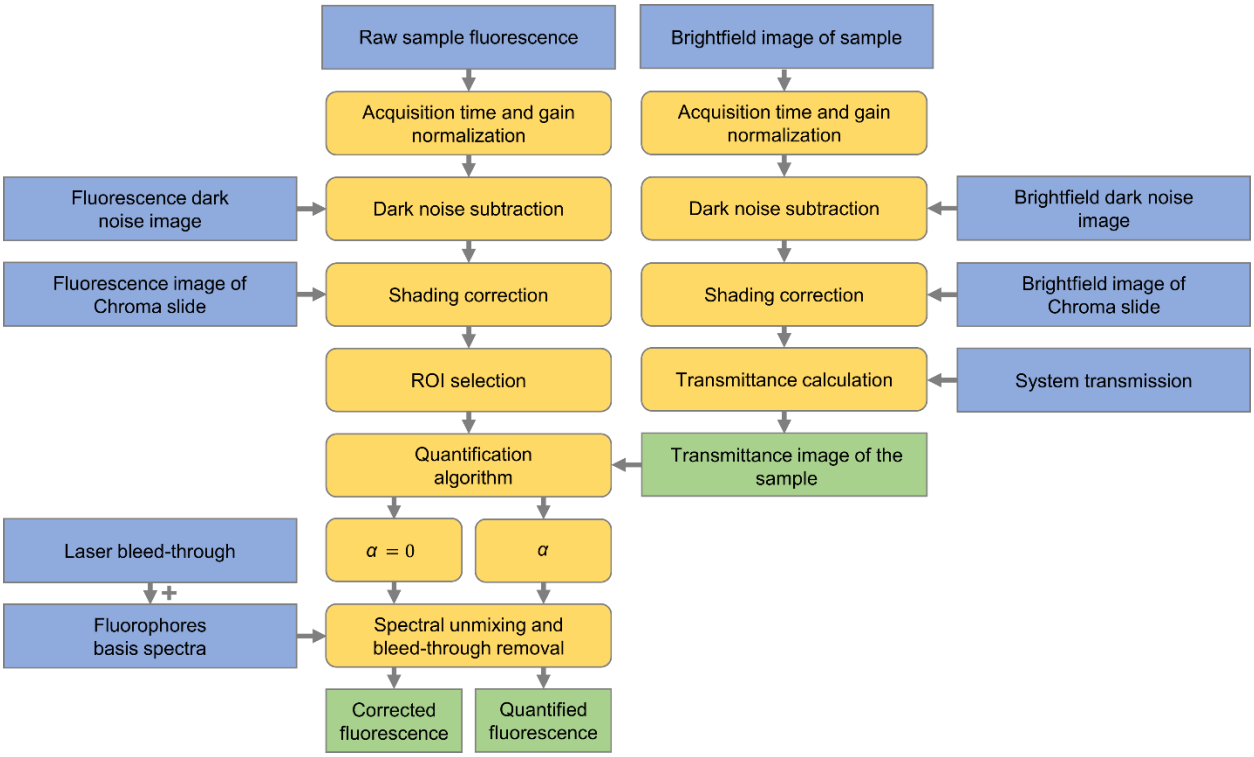

Figure 2. Image analysis steps to quantify the fluorescence emitted by the imaged sample using its transmittance measurement. Blue blocks represent experimental input images, yellow blocks represent image analysis steps performed on the acquired brightfield and fluorescence images of the sample, and green blocks represent output results. Details of each step are presented in the Experimental section.

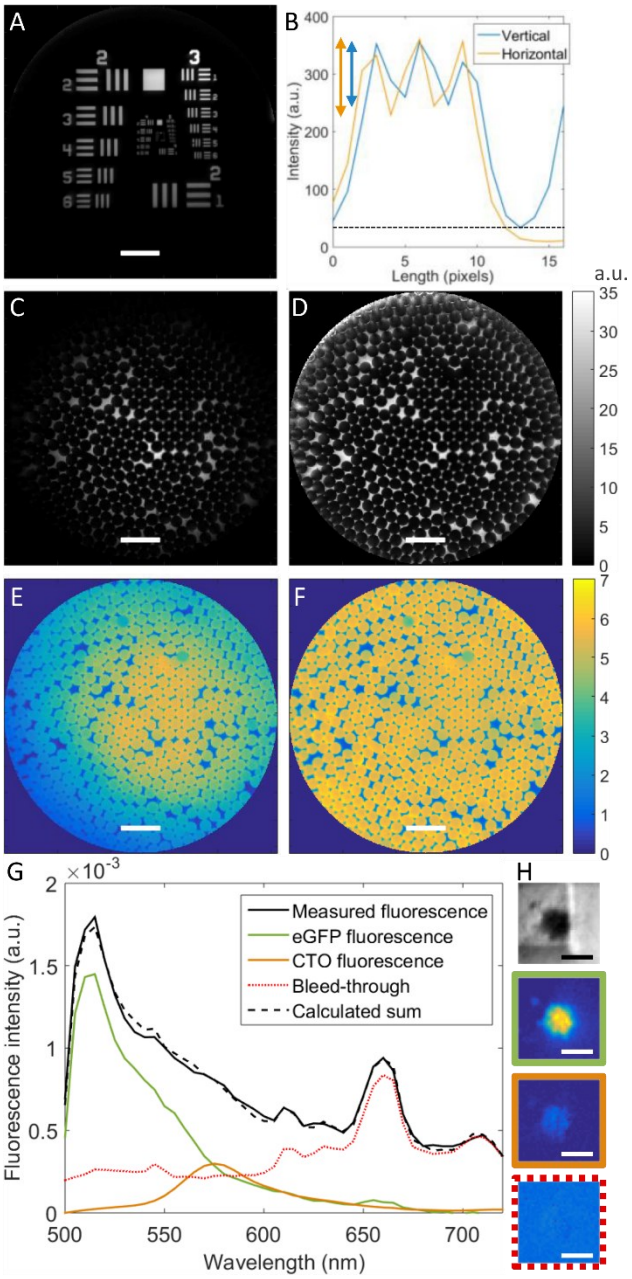

Figure 3. System characterization and image analysis steps. (A) Brightfield image (sum of wavelengths between 500 and 720 nm) of a 1951 USAF resolution target. Scale bar = 1 mm. (B) Average intensity profiles horizontally and vertically of the 3 lines of element 4, group 4 of the resolution target. Arrows show that the Rayleigh criterion of > 27% is respected. (C-D) Brightfield (a.u.) (at 720 nm) and (E-F) fluorescence (a. u.) images (at 610 nm) of a single layer of fluorescent beads before (C;E) and after (D;F) the shading correction. Scale bars = 1 mm. (G) Spectral unmixing of the eGFP and CTO fluorescence from the excitation laser bleed-through in a spheroid. (H) Top figure shows the brightfield image (at 720 nm) of the spheroid. Bottom three figures show the unmixed eGFP fluorescence (green perimeter) and CTO fluorescence (orange perimeter) from the laser bleed-through (red, ··· perimeter). Scale bars = 200 µm, a.u. is for arbitrary units.

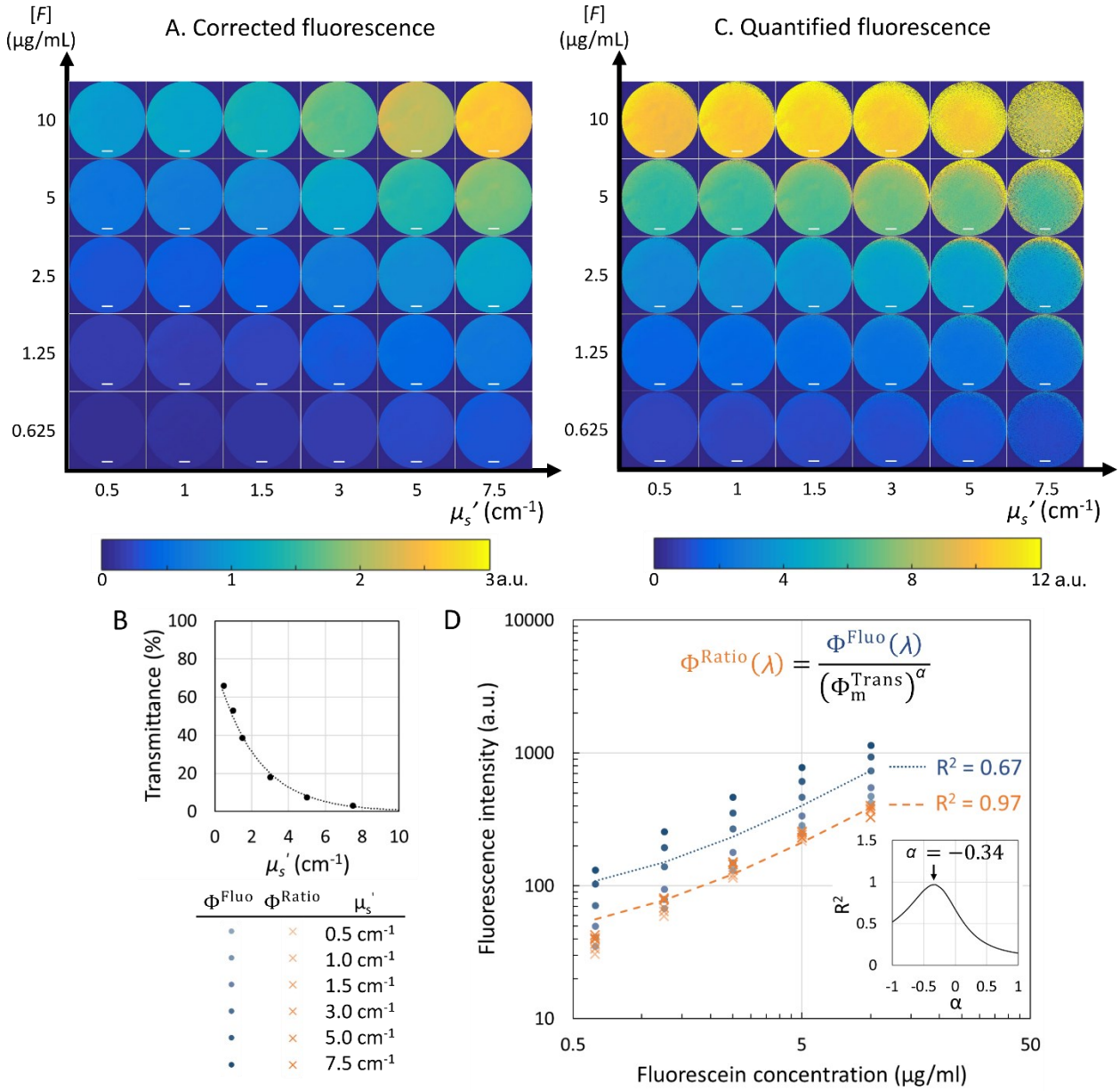

Figure 4. Optical phantom experiment. (A) Corrected fluorescence intensity images for 30 phantoms. (B) Mean transmittance of the phantoms with equal μ_s' values. Error bars (± standard deviation) are smaller than the size of the markers. (C) Quantified fluorescence intensity images of the same 30 phantoms. (D) Fluorescence quantification algorithm's performance to compensate for varying scattering coefficients. Raw fluorescence (blue, ●) and quantified fluorescence (orange, x) for μ_s' varying from 0.5 to 7.5 cm^{-1}. 7.5 cm^{-1} corresponds to the most saturated blue and orange while 0.5 cm^{-1} corresponds to the least saturated blue and orange. Insert shows the optimization of the geometry parameter α in relation to R^2. Scale bars = 1 mm, a.u. is for arbitrary units.

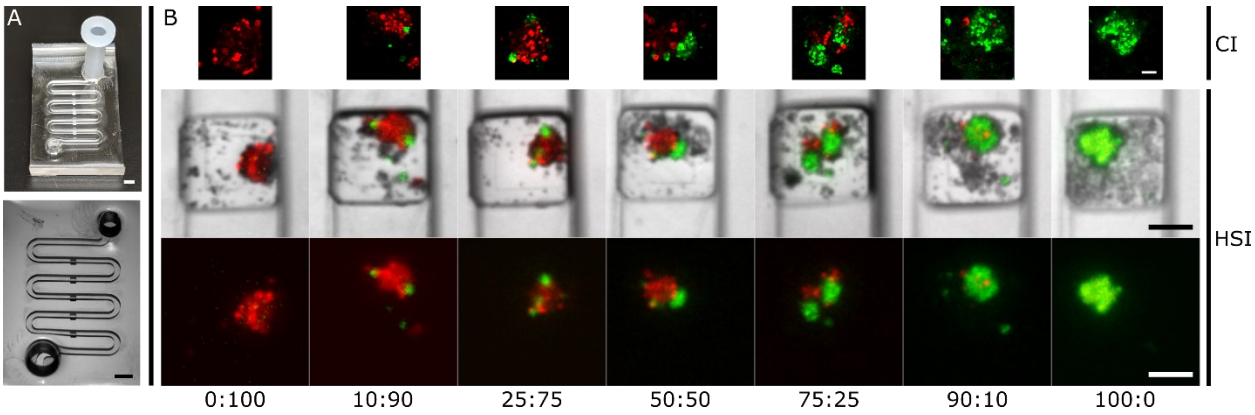

Figure 5. Fluorescence study of spheroids loaded on chip. (A) Microfluidic chip A. Top photograph shows chip A with an inlet inserted. Bottom photograph shows the tilted chip. Scale bars = 2 mm. (B) Visual comparison of confocal imaging (CI) and HSI of co-culture spheroids made with different ratios of eGFP-OV1946 and mCardinal-OV90. Top row shows maximum projections of confocal imaging of the same spheroids. Scale bar = 100 µm. Middle row shows brightfield (at 720 nm) overlaid with eGFP (at 515 nm) and mCardinal (at 685 nm) fluorescence. Bottom row shows only the fluorescence intensities of eGFP and mCardinal. Scale bars = 300 µm.

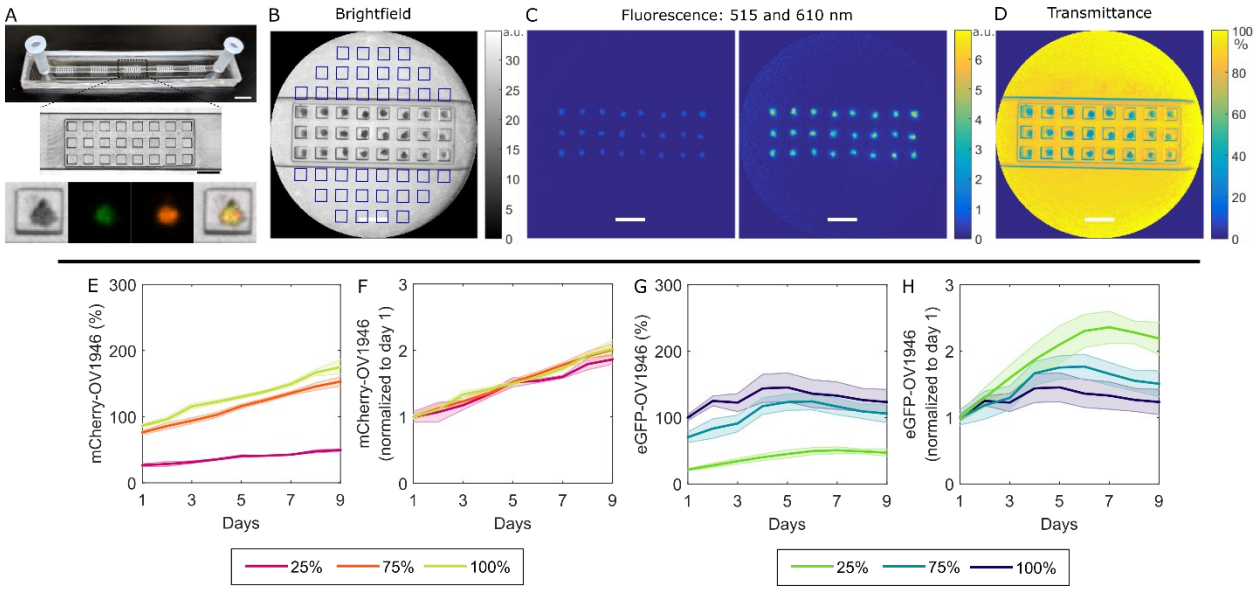

Figure 6. Fluorescence-based growth assay of spheroids formed on chip. (A) Microfluidic chip B. Top photograph shows chip B with inlets and outlets inserted. Scale bar = 6 mm. Middle phtograph shows a series of 24 wells. Scale bars = 1 mm. Bottom photographs show brightfield and fluorescence at 515 and 610 nm images and their overlay. (B-D) Brightfield (at 720 nm), fluorescence (at 515 and 610 nm) and transmittance (at 515 nm) imaging of 24 co-culture spheroids expressing eGFP and mCherry (ratio 25:75). Scale bars = 1 mm, a.u. is for arbitrary units. In (A), blue square shows an extrapolation of how many spheroids of the same size could be imaged if the microfluidic chip was optimized. (E-H) Growth assay quantifying each fluorescence subpopulation forming co-culture spheroids. Co-culture spheroids were formed by mixing two cell lines at specific ratios (100:0, 75:25, 25:75, and 0:100). Evolution over time of the initial percentage of mCherry-OV1946 (E) and eGFP-OV1946 (G) cells for each initial ratio. Day 1-normalized fluorescence intensity of mCherry-OV1946 (F) and eGFP-OV1946 (H). Shaded areas for each curve represents the standard error of the mean (n = 3).